PLOS ONE

RESEARCH ARTICLE

Multi-channel framelet denoising of diffusion-weighted images

Geng Chen[1☯], Jian Zhang[1,2☯], Yong Zhang[3], Bin Dong[4], Dinggang Shen[1,5]*, Pew-Thian Yap[1]*

1 Department of Radiology and Biomedical Research Imaging Center (BRIC) University of North Carolina, Chapel Hill, United States of America, **2** School of Information and Electrical Engineering, Hunan University of Science & Technology, Xiangtan, China, **3** Vancouver Research Center, Huawei, Burnaby, Canada, **4** Beijing International Center for Mathematical Research, Peking University, Beijing, China, **5** Department of Brain and Cognitive Engineering, Korea University, Seoul, Korea

☯ These authors contributed equally to this work.
* dgshen@med.unc.edu (DS); ptyap@med.unc.edu (PTY)

OPEN ACCESS

Citation: Chen G, Zhang J, Zhang Y, Dong B, Shen D, Yap P-T (2019) Multi-channel framelet denoising of diffusion-weighted images. PLoS ONE 14(2): e0211621. https://doi.org/10.1371/journal.pone.0211621

Editor: Dzung Pham, Center for Neuroscience and Regenerative Medicine, UNITED STATES

Received: May 29, 2018

Accepted: January 17, 2019

Published: February 6, 2019

Data Availability Statement: The synthetic data used in this study can be found at https://osf.io/57gcx/. The real data cannot be made publicly available as no such authorization was given by the Local Ethical Committee. Data are available upon request (contact with UNC IRB via irb_questions@unc.edu) to researchers qualified to handle confidential data.

Funding: This work was supported in part by NIH grants (NS093842 to Pew-Thian Yap, EB022880 to Pew-Thian Yap and Dinggang Shen, EB006733 to Dinggang Shen, EB009634 to Dinggang Shen,

Abstract

Diffusion MRI derives its contrast from MR signal attenuation induced by the movement of water molecules in microstructural environments. Associated with the signal attenuation is the reduction of signal-to-noise ratio (SNR). Methods based on total variation (TV) have shown superior performance in image noise reduction. However, TV denoising can result in stair-casing effects due to the inherent piecewise-constant assumption. In this paper, we propose a tight wavelet frame based approach for edge-preserving denoising of diffusion-weighted (DW) images. Specifically, we employ the unitary extension principle (UEP) to generate frames that are discrete analogues to differential operators of various orders, which will help avoid stair-casing effects. Instead of denoising each DW image separately, we collaboratively denoise groups of DW images acquired with adjacent gradient directions. In addition, we introduce a very efficient method for solving an ℓ_0 denoising problem that involves only thresholding and solving a trivial inverse problem. We demonstrate the effectiveness of our method qualitatively and quantitatively using synthetic and real data.

Introduction

Diffusion MRI affords in vivo insights into brain tissue microstructure and allows reconstruction of white matter pathways for neuroscience studies involving development, aging, and disorders [1–5]. However, since diffusion MRI derives its contrast from MR signal attenuation, it suffers from low signal-to-noise-ratio (SNR), which complicates subsequent quantitative analyses. To improve SNR, multiple repetitive scans are typically acquired and averaged for noise reduction. This however inevitably prolongs acquisition times and is hence prohibitive in clinical settings. Post-acquisition algorithms, such as total variation (TV) denoising [6], have been widely adopted due to their ability to remove noise without requiring additional acquisition time.

AG041721 to Dinggang Shen, and MH100217 to Dinggang Shen) and Hunan Provincial Education Department grant (15A066) to Jian Zhang. Bin Dong was supported in part by NSFC 11671022.

Competing interests: The authors have declared that no competing interests exist.

Diffusion-weighted (DW) images are typically acquired with non-collinear gradient directions. As shown in Fig 1, DW images that are scanned with similar gradient directions share a lot of commonalities. However, these commonalities diminish very quickly if the difference between the gradient directions increases. Denoising performance can be improved by making full use of information between images scanned with similar gradient directions; however, images scanned with very different gradient directions have to be avoided to reduce artifacts. We can also observe from the figure that the DW images are typically very noisy, indicating the great importance of denoising.

In this paper, we propose a group ℓ_0 minimization denoising framework that utilizes tight wavelet frames and takes advantage of the correlation between DW images scanned with neighboring gradient directions. The power of tight wavelet frames lies in their ability to sparsely approximate piecewise smooth functions and the existence of fast decomposition and reconstruction algorithms associated with them. In contrast, TV based methods are effective on restoring images that are piecewise constant, e.g., binary or cartoon-like images. They will, however, cause staircasing effects in images that are not piecewise constant [6].

TV denoising is typically realized by penalizing the ℓ_1-norm of image gradients. Instead of ℓ_1 regularization, which has been shown in the theory of compressed sensing [7] to produce sparse solutions, we opt to use ℓ_0 regularization. In [8], wavelet frame based ℓ_0 regularization shows better edge-preserving quality compared with the conventional ℓ_1 regularization. In [9], iterative hard thresholding algorithms show better performance than iterative soft thresholding algorithms. Based on these facts, we propose a group version of ℓ_0 minimization to take advantage of the correlation between DW images. Extensive experiments were carried out using synthetic data with different levels of noncentral chi (nc-χ) noise and real diffusion MRI data. The experimental results demonstrate that the proposed method outperforms TV denoising and non-local means (NLM) denoising [10]. Part of this work has been presented in a workshop [11]. Herein, we provide additional examples, results, derivations, and insights that are not part of the workshop publication. The rest of the paper is organized as follows: In Approach Section, we will provide detailed descriptions for our method. In Experiments Section, we will demonstrate the effectiveness of our method using extensive experiments on synthetic data and real data. In Discussion Section, we will provide in-depth discussions of our method. Finally, we will conclude this work in Conclusion Section.

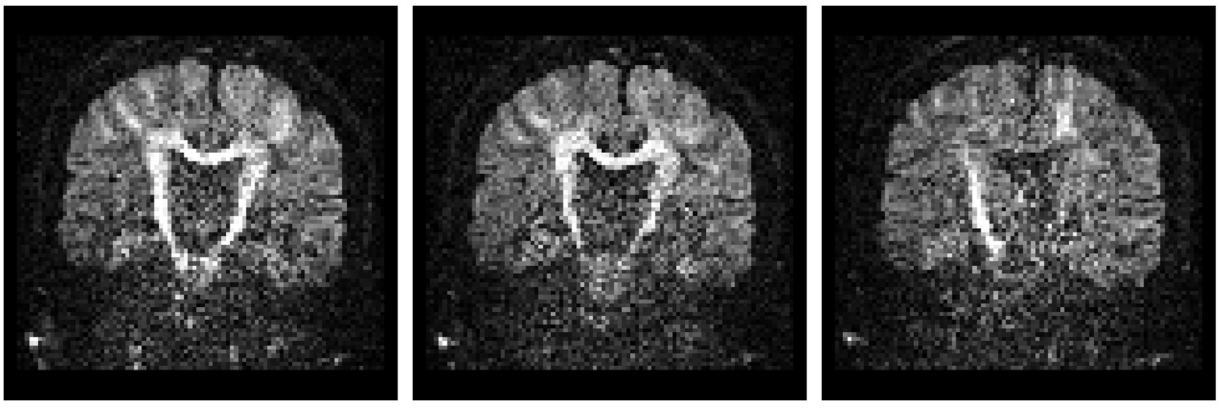

Fig 1. Diffusion-weighted images scanned at different gradient directions. The left and middle images were scanned with similar gradient directions. The right image was scanned at a nearly perpendicular gradient direction with respect to the reference.

https://doi.org/10.1371/journal.pone.0211621.g001

Approach

We will provide first a brief introduction to framelets, followed by details on how framelets can be incorporated into an ℓ_0 minimization framework for DWI denoising.

Tight framelets

A wavelet system $X \subset L_2(\mathbb{R})$ is called a tight wavelet frame of $L_2(\mathbb{R})$ [12] if

$$f = \sum_{g \in X} \langle f, g \rangle g, \quad \forall f \in L_2(\mathbb{R}), \tag{1}$$

where $\langle \cdot, \cdot \rangle$ is the inner product of $L_2(\mathbb{R})$. It is clear that an orthonormal basis is a tight frame, since the identity hold for arbitrary orthonormal bases in $L_2(\mathbb{R})$. When $X(\Psi)$ forms an orthonormal basis of $L_2(\mathbb{R})$, $X(\Psi)$ is called an orthonormal wavelet basis. Tight frames are generalization of orthonormal bases with greater redundancy—a property central to sparse representation and often desirable in applications such as denoising [13].

Given a set of generators $\Psi := \{\psi_1, \ldots, \psi_R\} \subset L_2(\mathbb{R}^d)$, which are desirably (anti)symmetric and compact functions, the corresponding quasi-affine system $X(\Psi)$ from level J is the collection of dilations and shifts of Ψ:

$$X(\Psi) = \{\psi_{l,r,k} : 1 \le r \le R; l, k \in \mathbb{Z}\}, \tag{2}$$

with

$$\psi_{l,r,k} := \begin{cases} 2^{\frac{l}{2}} \psi_r(2^l \cdot -k), & l \ge J, \\ 2^{\frac{l-J}{2}} \psi_r(2^l \cdot -2^{l-J}k), & l < J. \end{cases} \tag{3}$$

When $X(\Psi)$ forms a (tight) frame of $L_2(\mathbb{R})$, each function ψ_r, $r = 1, \ldots, R$, is called a (tight) framelet and the whole system $X(\Psi)$ is called a (tight) wavelet frame system. A tight wavelet frame is also called a Parseval frame. Note that in the literature the affine (or wavelet) system, which corresponds to the decimated wavelet (frame) transforms, is commonly used. The quasi-affine system above, introduced and analyzed in [14], corresponds to the undecimated wavelet (frame) transforms and essentially oversamples the wavelet frame system starting from level $J - 1$ and downwards. In this paper, we focus on the quasi-affine system because it has been shown to work better in image restoration [12]. We set $J = 0$ and consider only $l < 0$.

An approach to constructing framelets Ψ is by utilizing multiresolution analysis (MRA) [12]. One starts with a refinable function ϕ with refinement mask $a_0 \in \ell_2(\mathbb{Z})$ satisfying

$$\phi = 2 \sum_{k \in \mathbb{Z}} a_0[k] \phi(2 \cdot -k) \tag{4}$$

and $\hat{\phi}(0) = 1$, where $\hat{\phi}$ denotes Fourier transform of ϕ. The key is to find the masks $a_r \in \ell_2(\mathbb{Z})$ that gives

$$\psi_r = 2 \sum_{k \in \mathbb{Z}} a_r[k] \phi(2 \cdot -k), \quad r = 1, 2, \cdots, R. \tag{5}$$

The finite sequences $a_1, \ldots, a_R$ are called wavelet frame masks, or the high pass filters of the system. The refinement mask a_0 is also known as the low pass filter. The two equations above can be combined by defining $\psi_0 := \phi$. The unitary extension principle (UEP) [14] provides a general theory for constructing MRA-based tight wavelet frames. That is, as long as $\{a_1, \ldots, a_R\}$ are

finitely supported and their Fourier series satisfy

$$\sum_{r=0}^{R} |\hat{a}_r(\xi)|^2 = 1 \quad \text{and} \quad \sum_{r=0}^{R} \hat{a}_r(\xi)\overline{\hat{a}_r(\xi+\nu)} = 0, \tag{6}$$

for all $\nu \in \{0, \pi\}$ and $\xi \in [-\pi, \pi]$, the quasi-affine system $X(\Psi)$ forms a tight frame in $L_2(\mathbb{R})$.

For example, consider the centered B-splines of order p, i.e.,

$$\hat{\phi}(\xi) = e^{-ij\frac{\xi}{2}}\left(\frac{\sin(\xi/2)}{\xi/2}\right)^p, \tag{7}$$

with $j = 0$ when p is even and $j = 1$ when p is odd. The corresponding refinement mask is given as

$$\hat{a}_0(\xi) = e^{-ij\frac{\xi}{2}}\cos^p(\xi/2), \tag{8}$$

and the p wavelet masks as

$$\hat{a}_r(\xi) := -i^r e^{-ij\frac{\xi}{2}}\sqrt{\binom{p}{r}}\sin^r(\xi/2)\cos^{p-r}(\xi/2), \tag{9}$$

where $r = 1, 2, \ldots, p$. It is straightforward to show that the UEP conditions (6) are satisfied. Wavelet frame masks for $p = 1, 2, 4$ are shown in Table 1. It is worth noting that these masks corresponds to differential operators of various orders. For example, for piecewise linear B-spline, the masks a_1 and a_2 correspond to the first order and second order difference operators respectively up to a scaling factor.

When a tight wavelet frame is used, the given data is considered to be sampled as a local average

$$u[k] = \langle f, \phi(\cdot - k)\rangle. \tag{10}$$

Noting that [12]

$$\langle f, \psi_{l-1,r,k}\rangle = \sum_{k'\in\mathbb{Z}} a_{l,r}[k']\langle f, \psi_{l,0,k+k'}\rangle, \tag{11}$$

where the dilated sequence is defined as

$$a_{l,r}[k] = \begin{cases} a_r[2^l k], & k \in 2^{-l}\mathbb{Z}, \\ 0, & k \notin 2^{-l}\mathbb{Z}. \end{cases} \tag{12}$$

Table 1. Wavelet frame masks.

Piecewise Constant ($p = 1$)	Piecewise Linear ($p = 2$)	Piecewise Cubic ($p = 4$)
$a_0 = \frac{1}{2}[1, 1]$	$a_0 = \frac{1}{4}[1, 2, 1]$	$a_0 = \frac{1}{16}[1, 4, 6, 4, 1]$
$a_1 = \frac{1}{2}[1, -1]$	$a_1 = \frac{\sqrt{2}}{4}[1, 0, -1]$	$a_1 = \frac{1}{8}[-1, -2, 0, 2, 1]$
	$a_2 = \frac{1}{4}[-1, 2, -1]$	$a_2 = \frac{\sqrt{6}}{16}[1, 0, -2, 0, 1]$
		$a_3 = \frac{1}{8}[-1, 2, 0, -2, 1]$
		$a_4 = \frac{1}{16}[1, -4, 6, -4, 1]$

https://doi.org/10.1371/journal.pone.0211621.t001

The decomposition and reconstruction down to level $-L$ [12], i.e.,

$$\mathcal{P}_0 f = \mathcal{P}_{-L} f + \sum_{r=1}^{R} \sum_{j=-L}^{-1} \sum_{k\in\mathbb{Z}} \langle f, \psi_{r,j,k}\rangle \psi_{r,j,k}, \tag{13}$$

where

$$\mathcal{P}_l f = \sum_{r=1}^{R} \sum_{j<l} \sum_{k\in\mathbb{Z}} \langle f, \psi_{r,j,k}\rangle \psi_{r,j,k}, \tag{14}$$

can be realized with convolution using the masks. Denoting by W the L-level framelet decomposition, i.e.,

$$Wf = (\ldots, W_{l,r} f, \ldots)^\top \quad \text{for} \quad (l,r) \in \mathcal{B}_L, \tag{15}$$

with

$$\begin{aligned} \mathcal{B}_L \coloneqq \{&(1,1),(1,2),\cdots,(1,R),\\ &(2,1),\cdots,(L,R)\} \cup \{(L,0)\}, \end{aligned} \tag{16}$$

we have

$$W_{l,r} f = a_{-l,r} * a_{-l+1,0} * \cdots * a_{0,0} * f, \tag{17}$$

where $*$ denotes the convolution operator. If we use $W^\top$ to denote the framelet reconstruction, we have $W^\top W = I$, i.e., $f = W^\top W f$.

Given a 1-dimensional framelet system for $L_2(\mathbb{R})$, the d-dimensional tight wavelet frame system for $L_2(\mathbb{R}^d)$ can be easily constructed by using tensor products of the 1-dimensional framelets [12].

Problem formulation

Given a multi-channel or vector-valued image f of an arbitrary dimension with voxel $i \in \{1, \ldots, \mathrm{N}\}$ consisting of vector $f_i \in \Re^M$, where N is the number of voxels and M is the number of channels, we are interested in restoring its denoised counterpart u by solving the following problem:

$$\min_u \left\{ \Phi(u) = \| u - f \|_2^2 + \sum_{i,g,l,r} \lambda_{g,l,r} \left\| \sqrt{\sum_m w_{g,m}^2 \, \| \left(W_{l,r} u^{(m)}\right)_i \|_2^2} \right\|_0 \right\}. \tag{18}$$

Here, $u^{(m)}$ is the m-th channel of u. The regularization term is in fact a summation of G terms, each of which grouping a number of channels. The g-th grouping (with associated tuning parameter $\lambda_{g,l,r}$), where $g = \{1, 2, \ldots, G\}$, is defined according to the set of weights $\{w_{g,m}\}$, where $m \in \{1, 2, \ldots, M\}$. Channels with $w_{g,m} \neq 0$ are included in the grouping and their weighted framelet coefficients are jointly considered via ℓ_2-norm for penalization. The different groups can possibly overlap, implying that each channel can be included in different groups at the same time. This is in spirit similar to the overlapped group Lasso [15]. We

set

$$\lambda_{g,l,r} = \begin{cases} \lambda(\sum_m w_{g,m}^2)^{\frac{1}{2}}, & l, r \neq 0, \\ 0, & \text{otherwise.} \end{cases} \tag{19}$$

Here λ is a constant that can be set independently of the weights.

Optimization

Problem (18) can be solved effectively using penalty decomposition (PD) [16]. Defining auxiliary variables

$$(v_{g,m,l,r})_i \coloneqq w_{g,m}(W_{l,r}u^{(m)})_i, \tag{20}$$

this amounts to minimizing the following objective function with respect to u and $v \coloneqq \{v_{g,m,l,r}\}$:

$$\begin{aligned} L_\mu(u, v) = \quad & \| u - f \|_2^2 \sum_{i,g,l,r} \lambda_{g,l,r} \left\| \sqrt{\sum_m \| (v_{g,m,l,r})_i \|_2^2} \right\|_0 \\ & + \frac{\mu}{2} \sum_{i,g,m,l,r} \| w_{g,m}(W_{l,r}u^{(m)})_i - (v_{g,m,l,r})_i \|_2^2 . \end{aligned} \tag{21}$$

In PD, we (i) alternate between solving for u and v using block coordinate descent (BCD). Once this converges, we (ii) increase $\mu > 0$ by a multiplicative factor $\delta > 1$ and repeat step (i). This is repeated until increasing μ does not result in further changes to the solution [16]. See Algorithm 1 for a summary of the algorithm. Convergence analysis is provided in the S1 Appendix.

First subproblem. We solve for v in the first problem, i.e., $\min_v L_\mu(u, v)$. This is a group ℓ_0 problem and the solution can be obtained via hard-thresholding:

$$(v_{g,m,l,r})_i = \begin{cases} w_{g,m}(W_{l,r}u^{(m)})_i, & \text{if } (h_{g,l,r})_i \geq \dfrac{2\lambda_{g,l,r}}{\mu}, \\ 0, & \text{if otherwise,} \end{cases} \tag{22}$$

where

$$(h_{g,l,r})_i = \sum_{m'} \| w_{g,m'}(W_{l,r}u^{(m')})_i \|_2^2 . \tag{23}$$

This subproblem can be replaced using soft-thresholding to obtain an ℓ_1 version of the algorithm.

Second subproblem. By taking the partial derivative with respect to $u^{(m)}$, the solution to the second subproblem, i.e., $\min_u L_\mu(u, v)$, is for each m

$$\left(I + \frac{\mu}{2} \sum_{g,l,r} w_{g,m}^2 W_{l,r}^\top W_{l,r} \right) u^{(m)} = f^{(m)} + \frac{\mu}{2} \sum_{g,l,r} w_{g,m} W_{l,r}^\top v_{g,m,l,r}, \tag{24}$$

where we have dropped the subscript i for notation simplicity. Note that since we have

$\sum_{l,r} W_{l,r}^{\top} W_{l,r} = I$, the the problem can be simplified to

$$\left(1 + \frac{\mu}{2}\sum_{g} w_{g,m}^2\right) u^{(m)} = f^{(m)} + \frac{\mu}{2}\sum_{g,l,r} w_{g,m}\, W_{l,r}^{\top} v_{g,m,l,r}. \tag{25}$$

Solving the above equation for $u^{(m)}$ is trivial and involves only simple division.

Algorithm 1: Penalty Decomposition (PD)

Data : Multi-channel image f.
Parameters : Tuning parameter λ; initial penalty factor $\mu_0 > 0$; multiplicative factor $\delta > 1$; BCD tolerance ϵ_{BCD}; PD tolerance ϵ_{PD}.
Initialization : Iteration index $k = 0$; initial solution $u^{0,0}$; a constant $\Upsilon \geq \Phi(u^{0,0})$.
Output : Denoised image u.

/* Main Steps */

(1) For a fixed μ_k, obtain BCD solution (u^k, v^k) for $\min_{u,v} L_{\mu_k}(u, v)$. That is, set $k' = 0$ and iterate the following steps:

(1a) Solve $v^{k,k'+1} \in \arg\min_v L_{\mu_k}(u^{k,k'}, v)$.

(1b) Solve $u^{k,k'+1} = \arg\min_u L_{\mu_k}(u, v^{k,k'+1})$.

(1c) If $u^{k,k'+1}$ satisfies the BCD stopping criterion

$$\frac{\| u^{k,k'} - u^{k,k'+1} \|_2}{\max(\| u^{k,k'} \|_2, 1)} \leq \epsilon_{\text{BCD}},$$

set $(u^k, v^k) = (u^{k,k'+1}, v^{k,k'+1})$ and go to Step (2).

(1d) Set $k' \leftarrow k' + 1$ and go to Step (1).

(2) If u^k satisfies the PD stopping criterion

$$\frac{\| u^k - u^{k+1} \|_2}{\max(\| u^k \|_2, 1)} \leq \epsilon_{\text{PD}},$$

stop and output u^k. Otherwise, set $\mu_{k+1} = \delta\mu_k$.

(3) If $\min_v L_{\mu_{k+1}}(u^k, v) > \Upsilon$, set $u^{k+1,0} = u^{0,0}$. Otherwise, set $u^{k+1,0} = u^k$.

(4) Set $k \rightarrow k + 1$ and go to Step (1).

Setting the weights

In our case, each channel corresponds to a DW image. In setting the weights $\{w_{g,m}\}$, we note that the weights should decay with the dissimilarity between gradient directions associated with a pair of DW images. To reflect this, we let $G = M$ and set, for $g, m \in \{1, \ldots, M\}$,

$$w_{g,m} = \begin{cases} e^{\kappa[(v_m^{\top} v_g)^2 - 1]}, & |v_m^{\top} v_g| \geqslant \cos(\theta), \\ 0, & \text{otherwise}, \end{cases} \tag{26}$$

where $\kappa \geq 0$ is a parameter that determines the rate of decay of the weight. The exponential function is in fact modified from the probability density function of the Watson distribution [17] with concentration parameter κ. Essentially, this implies that for the g-th DW image acquired at gradient direction v_g, there is a corresponding regularization group that includes a set of images with associated weights $\{w_{g,m}\}$. The weight is maximal at $w_{g,g} = 1$ and is attenuated when $m \neq g$. Weights of images scanned at a gradient direction with angle greater than θ

in relation to v_g are set to 0, and the respective images are hence discarded from the group. We set $\theta = 30^{\circ}$.

Debiasing

The magnitude of the complex MR signal is commonly used because the phase of the complex signal is highly sensitive to many experimental factors [18, 19]. The magnitude MR signal is not affected by the phase error and it follows a nc-χ distribution [20, 21] rather than a Gaussian distribution and bias correction needs to be carried out especially when the SNR is low [18]. Bias correction can be performed before [22] or after [23] denoising. In our case, we adopted the latter for unbiased noise reduction [23].

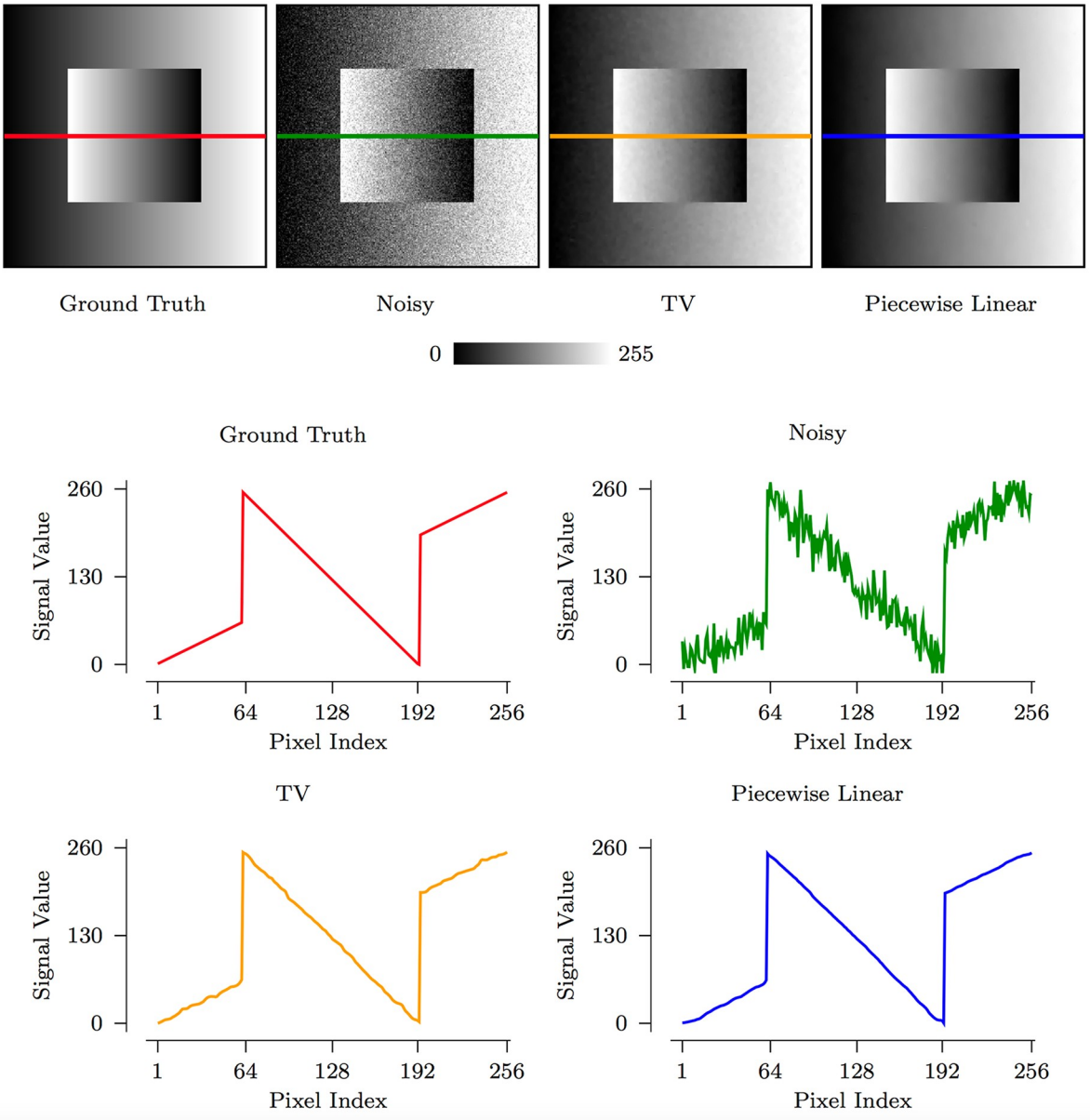

Fig 2. An illustration of how piecewise linear framelet denoising avoids the staircasing artifacts created by TV denoising.

https://doi.org/10.1371/journal.pone.0211621.g002

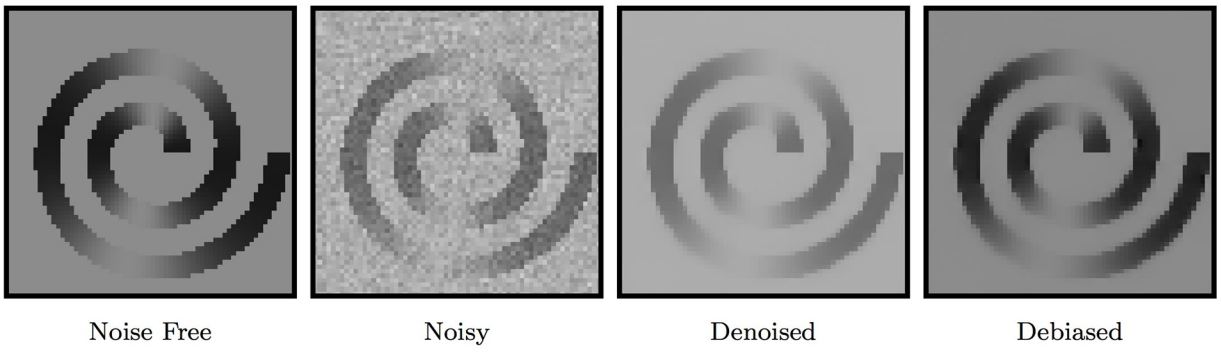

Fig 3. Debiasing the denoising outcome overcomes the noise floor and results in ($\sigma = 7.5$).

https://doi.org/10.1371/journal.pone.0211621.g003

Experiments

The main goal in the following experiments is to demonstrate that denoising performance can be improved by using

1. UEP-based tight wavelet frames, which avoids the staircasing effect;
2. ℓ_0 over ℓ_1 regularization;
3. Collaborative utilization of angularly neighboring DW images.

Unless stated otherwise, we used the piecewise linear tight wavelet frame with $L = 2$ levels of decomposition. The optimal λ values for ℓ_0 and ℓ_1 were in (1, 8], determined using grid search from 0.2 to 50 in steps of 0.2 based on the maximal peak signal-to-noise ratio (PSNR) defined

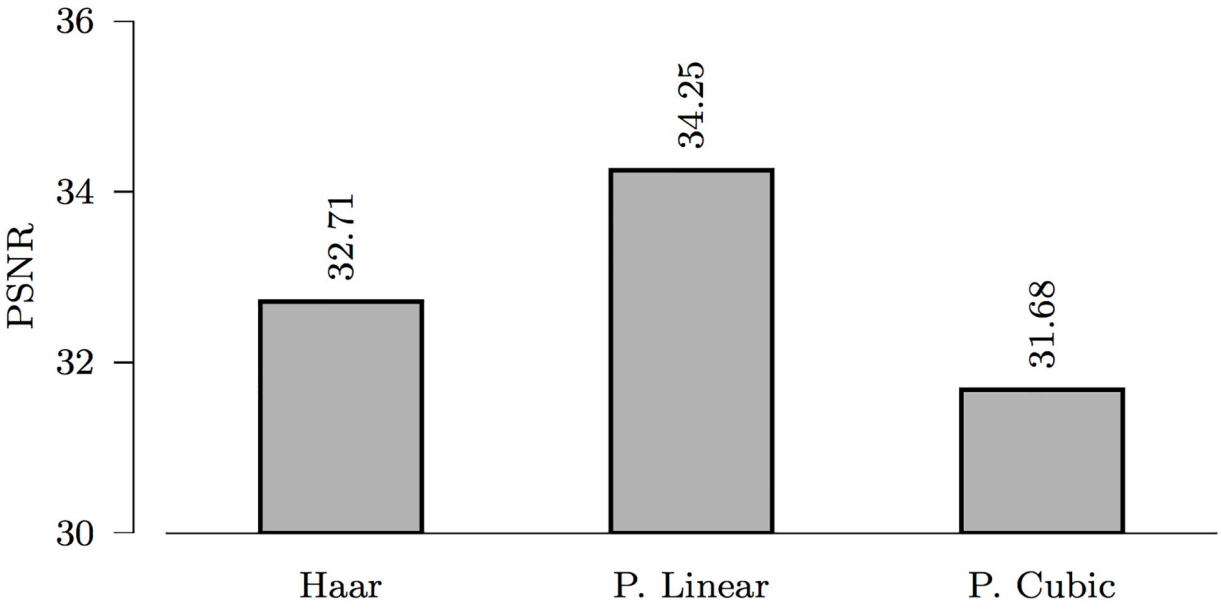

Fig 4. ℓ_0 denoising using Haar, piecewise linear, and piecewise cubic framelets ($L = 2$, $\sigma = 5$).

https://doi.org/10.1371/journal.pone.0211621.g004

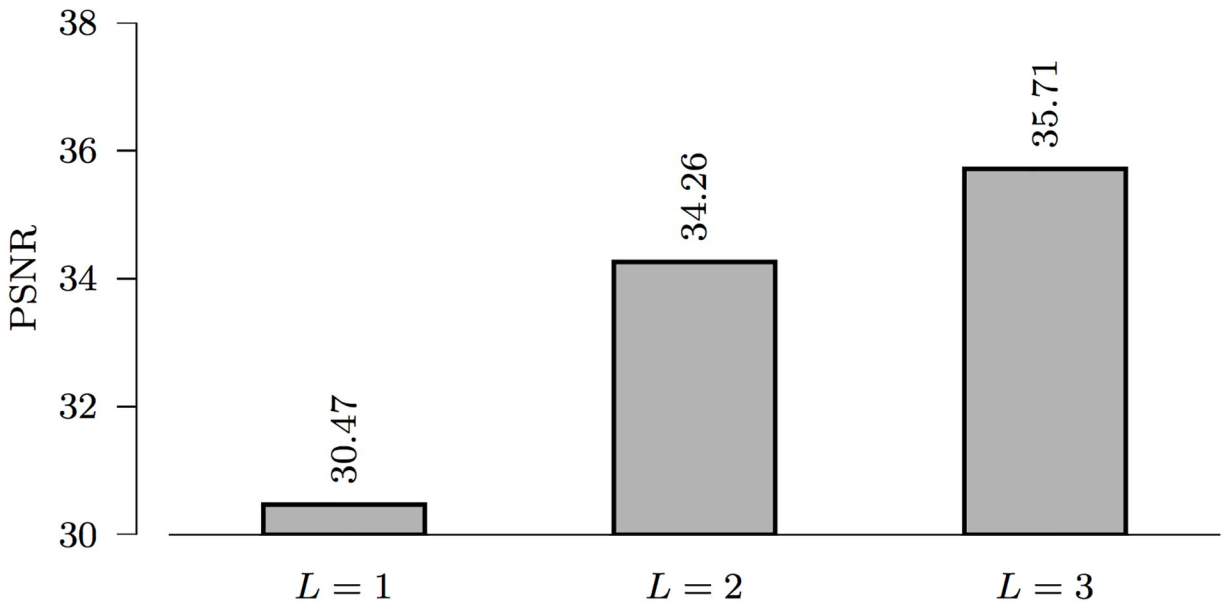

Fig 5. ℓ_0 denoising in relation to the level of decomposition, L (piecewise linear framelets, $\sigma = 5$).

https://doi.org/10.1371/journal.pone.0211621.g005

as

$$\mathrm{PSNR} = 10 \cdot \log_{10}\left(\frac{\mathrm{MAX}^2}{\mathrm{MSE}}\right), \tag{27}$$

where MAX is the maximal signal value and MSE is the mean square error.

For debiasing, the noise level is estimated from the image background using the method described in [24]. More advanced noise estimation methods [23, 25] can be used for improved accuracy.

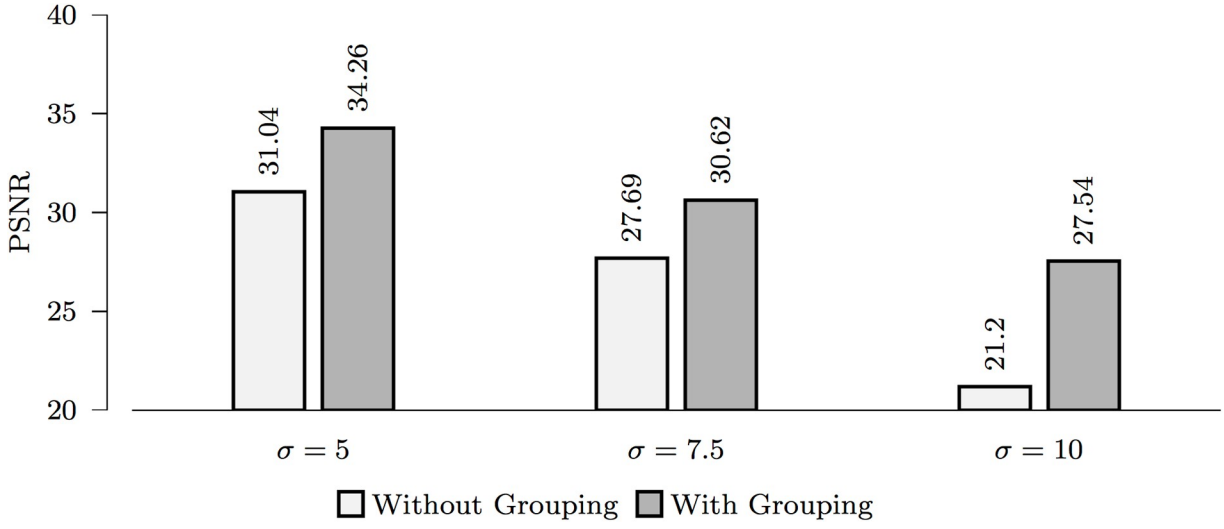

Fig 6. The effects of grouping on denoising.

https://doi.org/10.1371/journal.pone.0211621.g006

We utilized NLM filtering as a comparison baseline. Following the work presented in [26], we set the patch radius to 1 and search radius to 2.

Datasets

Spiral data. A synthetic dataset of a spiral was generated for quantitative evaluation. The parameters used for synthetic data simulation were consistent with the real data described next: $b = 2000\text{s/mm}^3$, 48 gradient directions, $64 \times 64 \times 16$ voxels with resolution $2 \times 2 \times 2$ mm^3. Three levels of 32-channel nc-χ noise [27] was added: $\sigma = 5$, 7.5, and 10, corresponding to SNR = 30, 20, 10. SNR is defined as η/σ [28], where η is the true signal value, which in our case is the white matter non-DW signal. The varying curvature reflects the various degree of bending of white matter pathways and gives us a good basis for evaluating how denoising performance changes in different conditions.

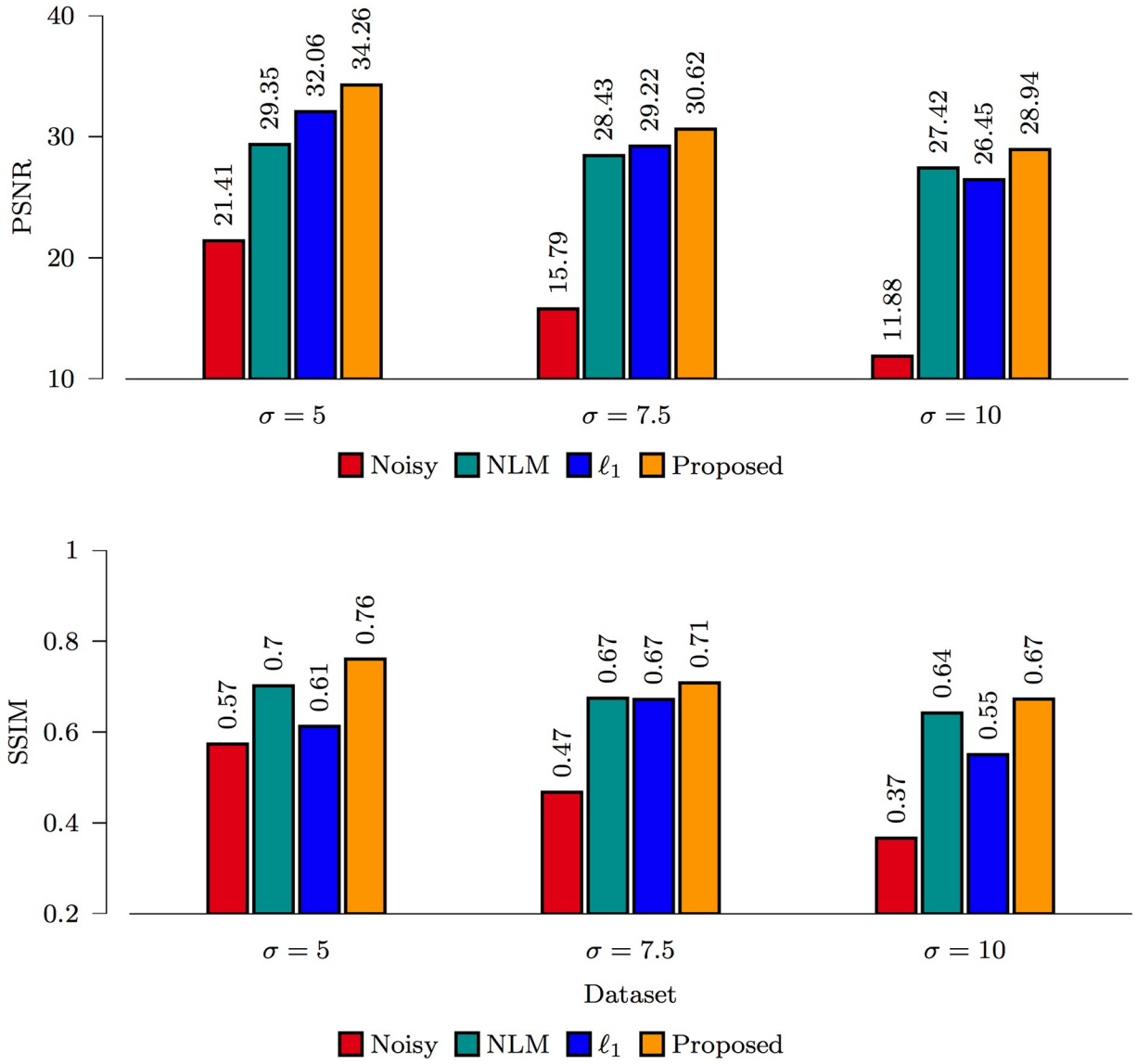

Fig 7. Performance comparison based on the spiral data.

https://doi.org/10.1371/journal.pone.0211621.g007

ISBI phantom. Evaluation was also performed using the realistic diffusion MRI phantom adopted in the ISBI 2013 HARDI challenge (http://hardi.epfl.ch/static/events/2013_ISBI/). A python package, called phantomαs [29], was used to generate the noise free phantom, with gradient directions and diffusion weighting consistent with the spiral data described above. Three levels of 32-channel nc-χ noise, similar to the spiral data, was added to the noise free phantom.

Real data. DW images were acquired using Siemens 3T TRIO MR scanner with the same gradient directions and b-value as the spiral data. The imaging protocol is as follows: 128 × 96 imaging matrix, voxel size of 2 × 2 × 2 mm^3, TE = 97 ms, TR = 11, 300 ms, 32-channel receiver coil. Imaging acquisition was repeatedly performed on the same subject for 8 times. We averaged the 8 sets of DW images and removed the nc-χ noise bias to obtain the ground truth for

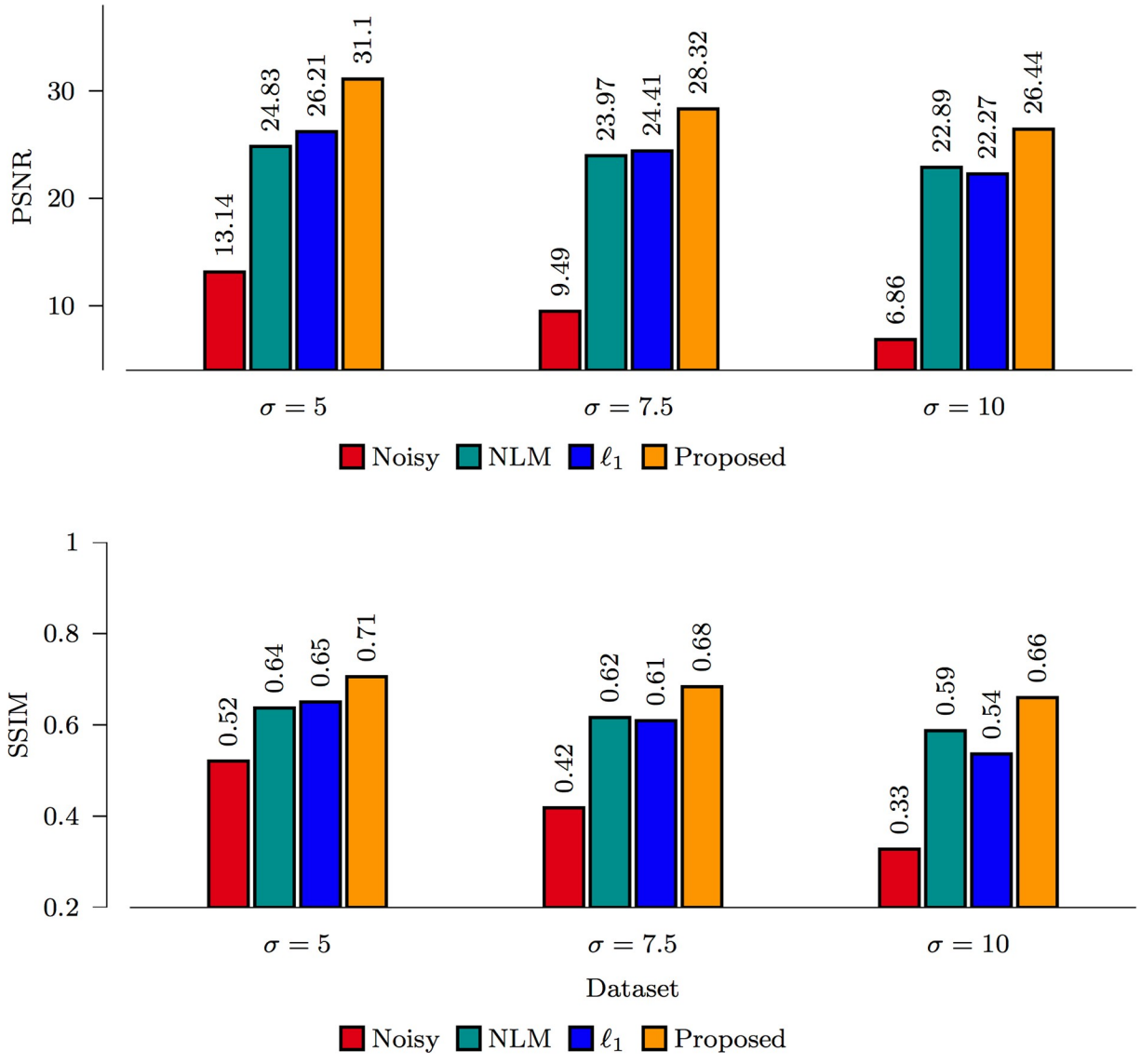

Fig 8. Performance comparison based on the ISBI phantom.

https://doi.org/10.1371/journal.pone.0211621.g008

evaluation. Informed written consent was obtained from the subject and the experimental protocol was approved by the Institutional Review Board of the University of North Carolina (UNC) School of Medicine. The study was carried out in accordance with the approved guidelines.

Results

The staircasing effect. The staircasing effect is often observed in denoising based on TV regularization [30]. The power of tight wavelet frames lies in their ability to sparsely approximate piecewise smooth functions. They are hence better suited for images with gradual intensity changes. In Fig 2, we show an example of how piecewise linear framelet denoising avoids the staircasing effect and results in a smoother image without blocking artifacts. In contrast, TV denoising causes patch artifacts when the image is not piecewise constant.

Bias correction. The noise-induced bias on the estimated magnitude signal is especially prominent when the diffusion weighting is high. We removed the nc-χ bias using the method described in [27]. Fig 3 indicates that the nc-χ noise results in a noise floor especially when the

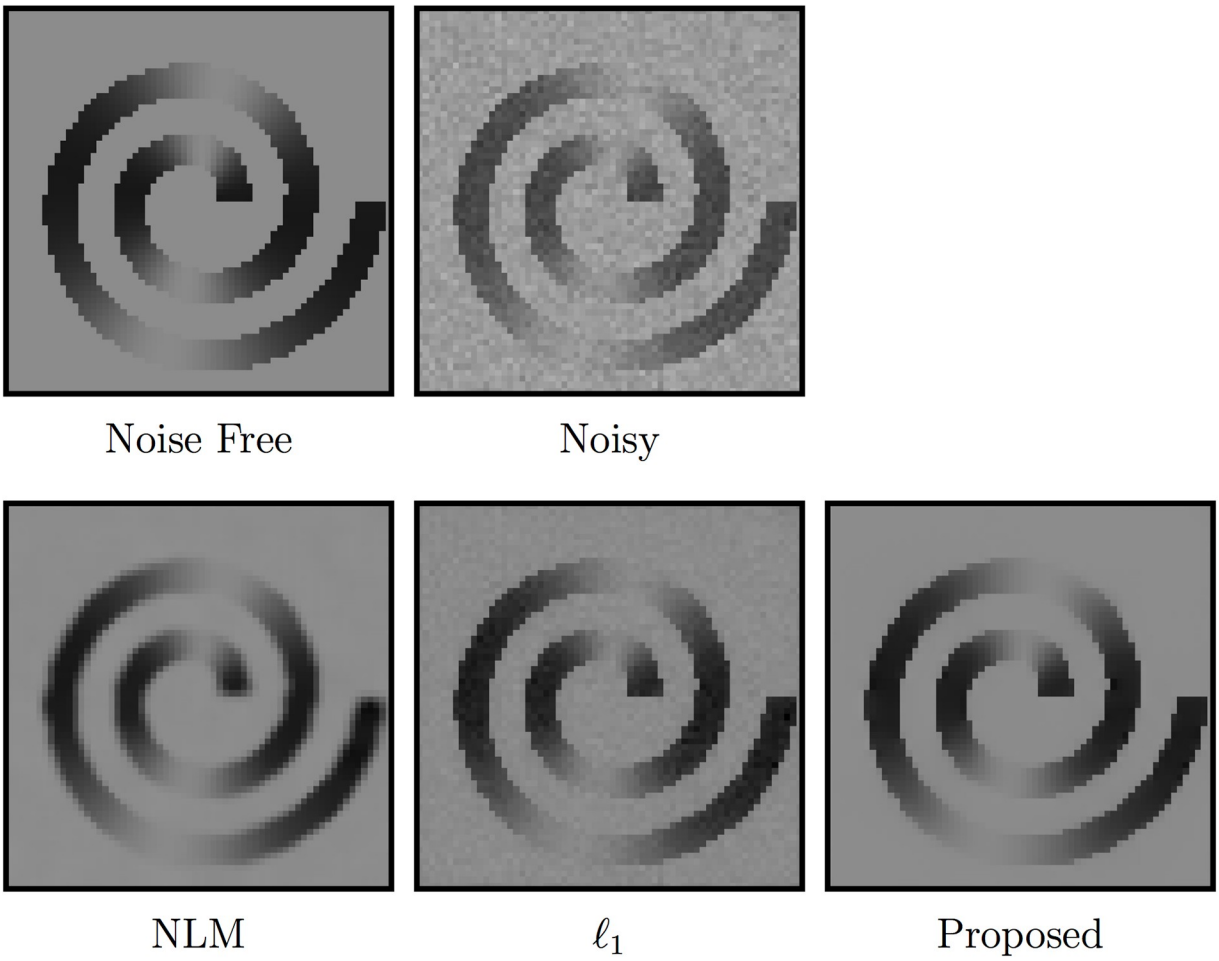

Fig 9. Comparison of denoised DW images given by different methods ($\sigma = 5$).

https://doi.org/10.1371/journal.pone.0211621.g009

signal is low [27]. This manifests as elevation of intensity value after denoising. Removing the noise bias produces an image that is closer to the ground truth.

Type of framelets and number of levels. Using the spiral data for evaluation, our results shown in Fig 4 indicate that piecewise linear framelet denoising performs better than other types of framelets.

Fig 5 indicates that denoising performance improves with the increase in the number of levels, L. However, the time cost increases dramatically with L, i.e., 27 s for $L = 1$, 29 s for $L = 2$, and 378 s for $L = 3$ (based on a 4-core Intel i7 processor). Therefore, we choose $L = 2$ for reasonable denoising performance with a reasonable time cost.

Effects of grouping. Fig 6 shows the results of denoising with and without grouping of angularly neighboring images. Grouping can be observed to significantly improve PSNR.

Comparison between methods. The PSNR and SSIM [31] results for the spiral data and ISBI phantom, shown in Figs 7 and 8, indicate that the proposed ℓ_0-based framelet method gives the best performance for all noise levels. The DW images, shown in Figs 9 and 10, indicate that both ℓ_1 and ℓ_0 give sharper edges compared with NLM. Noise, however, is not totally removed for the case of ℓ_1. Only ℓ_0 is able to effectively remove noise and preserve edges. Note that, for both synthetic and real data, nc-χ bias was removed using the method described in [27].

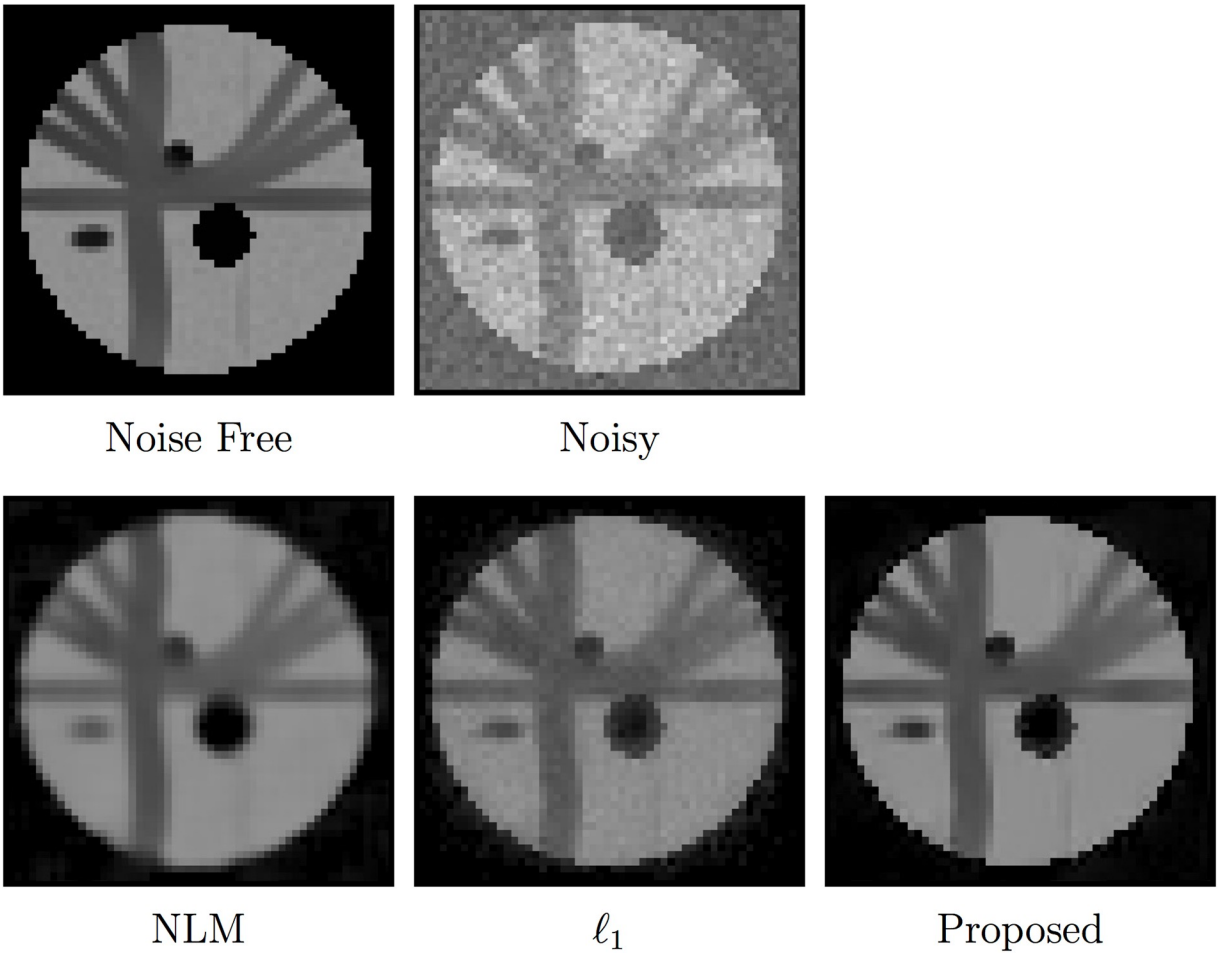

Fig 10. Comparison of denoised DW images given by different methods ($\sigma = 7.5$).

https://doi.org/10.1371/journal.pone.0211621.g010

Table 2. Computation times.

	NLM	ℓ_1	Proposed
Time (sec)	186	34	27

https://doi.org/10.1371/journal.pone.0211621.t002

We also compared the computational times of different methods using the spiral data with a computer equipped with a 4-core Intel i7 processor. The results, shown in Table 2, indicate that our method and ℓ_1 perform more efficiently than NLM.

Real data. For the real data, we used the average image as the ground truth for quantitative evaluations. The results for all 8 datasets, shown in Fig 11, are consistent with Figs 7 and 8, indicating that ℓ_0 gives the best performance. The visual results in Fig 12 indicate that the results given by ℓ_0 is closest to the ground truth. This is confirmed by the root-mean-square

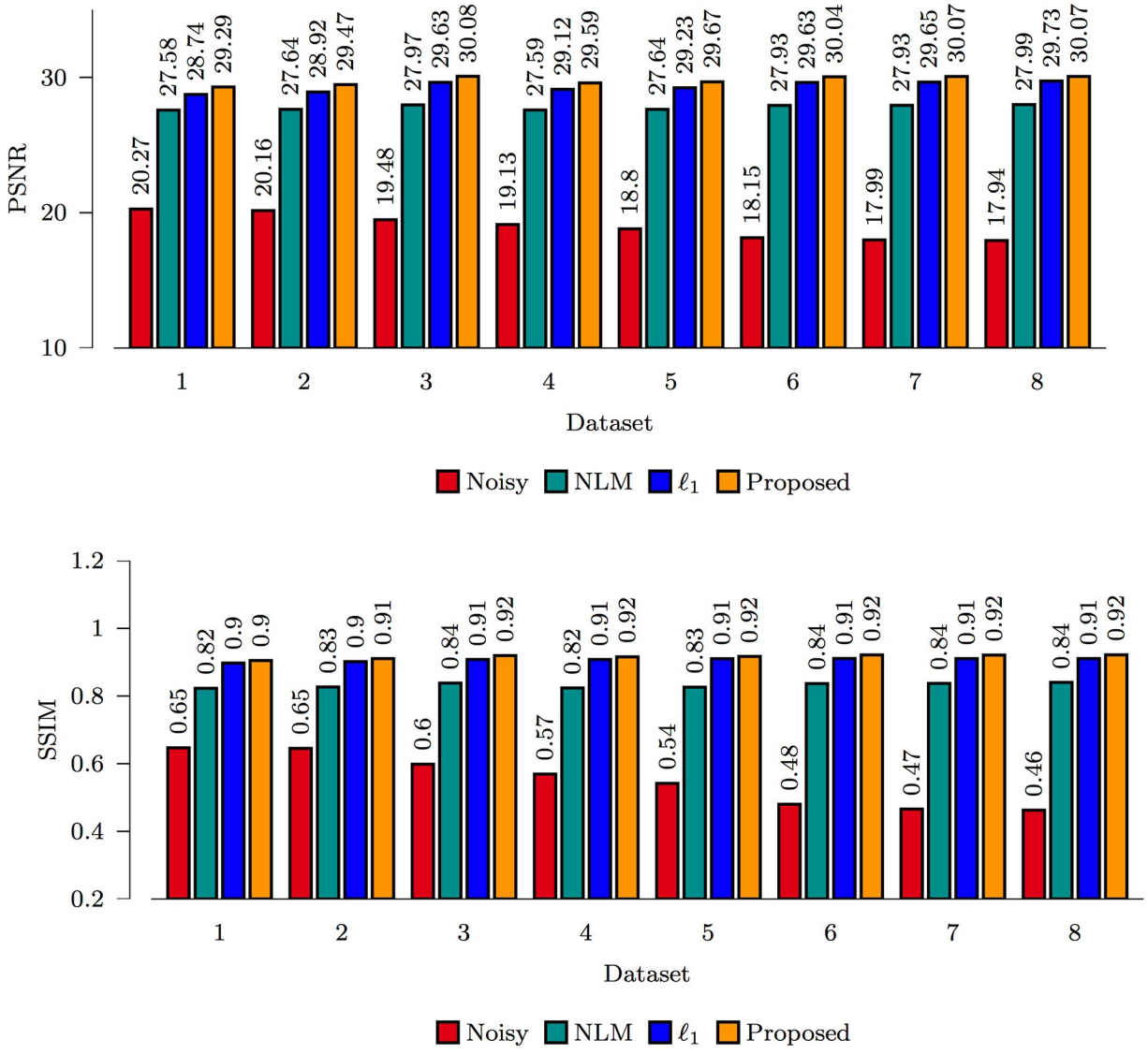

Fig 11. Performance comparison based on the real data.

https://doi.org/10.1371/journal.pone.0211621.g011

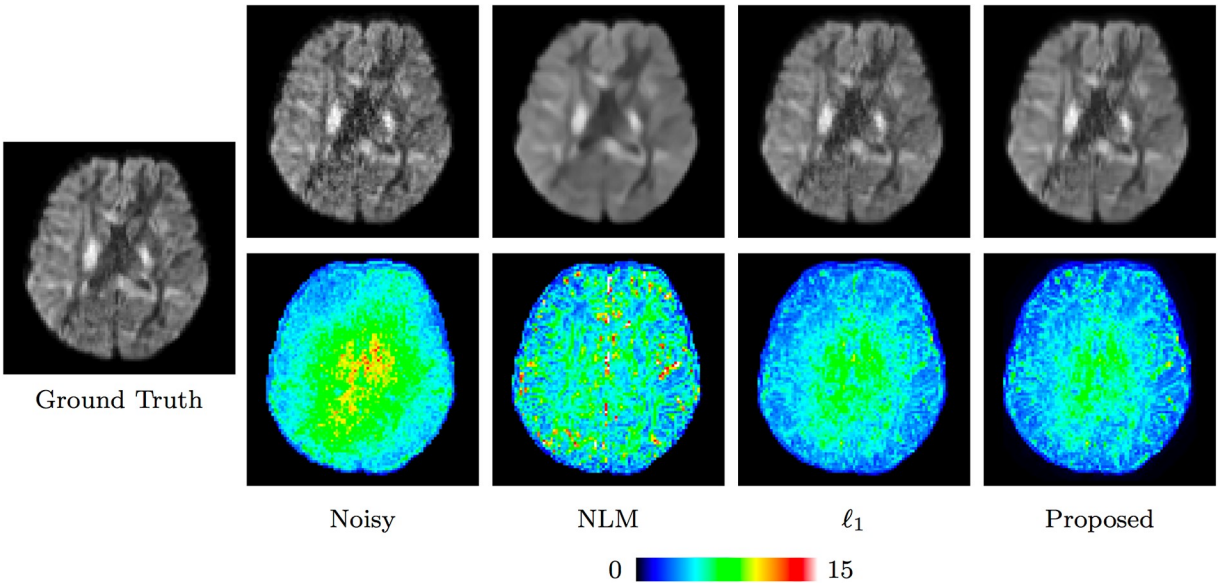

Fig 12. Comparison of denoised DW images using the real data.

https://doi.org/10.1371/journal.pone.0211621.g012

error (RMSE) map computed between the denoised data and the ground truth data. In contrast, NLM over-smooths the image and edge information is hence lost.

Discussion

In this paper, we have introduced a method that harnesses correlations between DW images scanned with similar gradient directions for effective edge-preserving denoising. Our main contributions lie in three aspects. Firstly, UEP was employed to generate frames that were discrete analogues to differential operators of various orders; Secondly, instead of the conventional ℓ_1 regularization, a very efficient method was proposed in order to solve an ℓ_0 denoising problem that involves only thresholding and a trivial inverse problem; Thirdly, DW images acquired using neighboring gradient directions were used for collaborative denoising.

NLM was used as a comparison baseline in our evaluation. However, similar to [22, 32], we found the performance of NLM to be unsatisfactory. NLM can be improved by designing better metrics for patch matching, instead of the conventional Euclidean distance. For instance, inspired by the human visual system, Foi and Boracchi [33] proposed a patch foveation operator for measuring patch distance. Baselice [34] proposed to measure pixel using the Kolmogorov—Smirnov distance, showing promising performance in reducing speckle noise in ultrasound images. NLM can be further improved by extending its search volume. For instance, collaborative NLM [35] extended the search volume to a number of co-denoising images to enrich the similar information used in noise reduction. Chen et al. [36, 37] proposed to improve NLM by considering the similar information in both spatial domain and diffusion wavevector domain. This idea was further employed to improve atlas building [38] and resolution enhancement [39].

Conclusion

In conclusion, we have proposed a method to remove the noise in DW images. The proposed method takes advantage of multi-channel framelet and the correlations among DW images for

effective noise removal. The associated ℓ_0 optimization problem is solved by an effective iterative hard thresholding algorithm. Extensive experiments on synthetic data and real data demonstrate the advantage of our method over various noise reduction methods, including TV regularization, NLM, and the ℓ_1 counterpart of our method.

Supporting information

S1 Appendix. Proof of convergence.
(PDF)

Acknowledgments

This work was supported in part by NIH grants (NS093842, EB022880, EB006733, EB009634, AG041721, and MH100217) and Hunan Provincial Education Department grant (15A066). Bin Dong was supported in part by NSFC 11671022.

Author Contributions

Conceptualization: Yong Zhang, Bin Dong, Pew-Thian Yap.

Data curation: Geng Chen.

Formal analysis: Geng Chen.

Funding acquisition: Jian Zhang, Bin Dong, Dinggang Shen, Pew-Thian Yap.

Investigation: Jian Zhang.

Methodology: Yong Zhang, Bin Dong, Pew-Thian Yap.

Project administration: Dinggang Shen, Pew-Thian Yap.

Resources: Dinggang Shen, Pew-Thian Yap.

Software: Pew-Thian Yap.

Supervision: Dinggang Shen, Pew-Thian Yap.

Validation: Jian Zhang.

Visualization: Geng Chen.

Writing – original draft: Jian Zhang, Pew-Thian Yap.

Writing – review & editing: Geng Chen, Pew-Thian Yap.

References

1. Yap PT, Fan Y, Chen Y, Gilmore J, Lin W, Shen D. Development Trends of White Matter Connectivity in the First Years of Life. PLoS ONE. 2011; 6(9):e24678. https://doi.org/10.1371/journal.pone.0024678 PMID: 21966364
2. Wee CY, Yap PT, Li W, Denny K, Brownyke JN, Potter GG, et al. Enriched White-Matter Connectivity Networks for Accurate Identification of MCI Patients. NeuroImage. 2011; 54(3):1812–1822. https://doi.org/10.1016/j.neuroimage.2010.10.026 PMID: 20970508
3. Wee CY, Yap PT, Zhang D, Denny K, Browndyke JN, Potter GG, et al. Identification of MCI Individuals Using Structural and Functional Connectivity Networks. NeuroImage. 2012; 59(3):2045–2056. https://doi.org/10.1016/j.neuroimage.2011.10.015 PMID: 22019883
4. Wee CY, Wang L, Shi F, Yap PT, Shen D. Diagnosis of Autism Spectrum Disorders Using Regional and Interregional Morphological Features. Human Brain Mapping. 2014; 35(7):3414–3430. https://doi.org/10.1002/hbm.22411 PMID: 25050428

5. Jin Y, Wee CY, Shi F, Thung KH, Yap PT, Shen D. Identification of Infants at High-Risk for Autism Spectrum Disorder Using Multi-Parameter Multi-Scale White Matter Connectivity Networks. Human Brain Mapping. 2015; 36(12):4880–4896. https://doi.org/10.1002/hbm.22957 PMID: 26368659
6. Ring W. Structural Properties of Solutions to Total Variation Regularization Problems. Mathematical Modelling and Numerical Analysis. 2000; 34:799–810. https://doi.org/10.1051/m2an:2000104
7. Candès EJ, Romberg J, Tao T. Robust uncertainty principles: Exact signal reconstruction from highly incomplete frequency information. IEEE Transactions on Information Theory. 2006; 52(2):489–509. https://doi.org/10.1109/TIT.2005.862083
8. Zhang Y, Dong B, Lu Z. ℓ_0 Minimization for wavelet frame based image restoration. Mathematics of Computation. 2013; 82:995–1015. https://doi.org/10.1090/S0025-5718-2012-02631-7
9. Chan RH, Chan TF, Shen L, Shen Z. Wavelet algorithms for high-resolution image reconstruction. SIAM Journal on Scientific Computing. 2003; 24(4):1408–1432. https://doi.org/10.1137/S1064827500383123
10. Buades A, Coll B, Morel JM. A review of image denoising algorithms, with a new one. Multiscale Modeling & Simulation. 2005; 4(2):490–530. https://doi.org/10.1137/040616024
11. Zhang J, Chen G, Zhang Y, Dong B, Shen D, Yap PT. Denoising Diffusion-Weighted Images Using Grouped Iterative Hard Thresholding of Multi-Channel Framelets. In: MICCAI Workshop on Computational Diffusion MRI (CDMRI); 2016. p. 49–59.
12. Dong B, Shen Z. MRA-Based Wavelet Frames and Applications. In: IAS Lecture Notes Series, Summer Program on "The Mathematics of Image Processing". Park City Mathematics Institute; 2010.
13. Mallat S. A Wavelet Tour of Signal Processing: The Sparse Way. Third edition ed. Academic Press; 2008.
14. Ron A, Shen Z. Affine systems in $L_2(\mathbb{R}^d)$: The analysis of the analysis operator. Journal of Functional Analysis. 1997; 148(2):408–447. https://doi.org/10.1006/jfan.1996.3079
15. Jacob L, Obozinski G, Vert JP. Group lasso with overlap and graph lasso. In: Proceedings of the 26th annual international conference on machine learning. ACM; 2009. p. 433–440.
16. Lu Z, Zhang Y. Sparse approximation via penalty decomposition methods. SIAM Journal on Optimization. 2013; 23(4):2448–2478. https://doi.org/10.1137/100808071
17. Schwartzman A, Dougherty RF, Taylor JE. False Discovery Rate Analysis of Brain Diffusion Direction maps. Annals of Applied Statistics. 2008; 2(1):153–175. https://doi.org/10.1214/07-AOAS133
18. Henkelman RM. Measurement of signal intensities in the presence of noise in MR images. Medical Physics. 1985; 12(2):232–233. https://doi.org/10.1118/1.595711 PMID: 4000083
19. Liu J, Koenig JL. An automatic phase correction method in nuclear magnetic resonance imaging. Journal of Magnetic Resonance (1969). 1990; 86(3):593–604. https://doi.org/10.1016/0022-2364(90)90036-9
20. Koay CG, Basser PJ. Analytically exact correction scheme for signal extraction from noisy magnitude MR signals. Journal of Magnetic Resonance. 2006; 179(2):317–322. https://doi.org/10.1016/j.jmr.2006.01.016 PMID: 16488635
21. Constantinides CD, Atalar E, McVeigh ER. Signal-to-noise measurements in magnitude images from NMR phased arrays. Magnetic Resonance in Medicine. 1997; 38(5):852–857. https://doi.org/10.1002/mrm.1910380524 PMID: 9358462
22. St-Jean S, Coupé P, Descoteaux M. Non Local Spatial and Angular Matching: Enabling higher spatial resolution diffusion MRI datasets through adaptive denoising. Medical Image Analysis. 2016; 32:115–130. https://doi.org/10.1016/j.media.2016.02.010 PMID: 27082655
23. Veraart J, Fieremans E, Novikov DS. Diffusion MRI noise mapping using random matrix theory. Magnetic Resonance in Medicine. 2016; 76(5):1582–1593. https://doi.org/10.1002/mrm.26059 PMID: 26599599
24. Manjón JV, Carbonell-Caballero J, Lull JJ, García-Martí G, Martí-Bonmatí L, Robles M. MRI denoising using non-local means. Medical Image Analysis. 2008; 12(4):514–523. https://doi.org/10.1016/j.media.2008.02.004 PMID: 18381247
25. St-Jean S, De Luca A, Viergever MA, Leemans A. Automatic, Fast and Robust Characterization of Noise Distributions for Diffusion MRI. In: Frangi AF, Schnabel JA, Davatzikos C, Alberola-López C, Fichtinger G, editors. Medical Image Computing and Computer Assisted Intervention (MICCAI). Cham: Springer International Publishing; 2018. p. 304–312.
26. Manjón JV, Coupé P, Martí-Bonmatí L, Collins DL, Robles M. Adaptive non-local means denoising of MR images with spatially varying noise levels. Journal of Magnetic Resonance Imaging. 2010; 31(1):192–203. https://doi.org/10.1002/jmri.22003 PMID: 20027588

27. Koay CG, Özarslan E, Basser PJ. A signal transformational framework for breaking the noise floor and its applications in MRI. Journal of Magnetic Resonance. 2009; 197(2):108–119. https://doi.org/10.1016/j.jmr.2008.11.015 PMID: 19138540

28. Gudbjartsson H, Patz S. The Rician distribution of noisy MRI data. Magnetic Resonance in Medicince. 1995; 34:910–914. https://doi.org/10.1002/mrm.1910340618

29. Caruyer E, Daducci A, Descoteaux M, Houde JC, Thiran JP, Verma R. Phantomas: a flexible software library to simulate diffusion MR phantoms. In: ISMRM; 2014.

30. Knoll F, Bredies K, Pock T, Stollberger R. Second order total generalized variation (TGV) for MRI. Magnetic Resonance in Medicince. 2011; 65(2):480–491. https://doi.org/10.1002/mrm.22595

31. Wang Z, Bovik AC, Sheikh HR, Simoncelli EP. Image quality assessment: from error visibility to structural similarity. IEEE Transactions on Image Processing. 2004; 13(4):600–612. https://doi.org/10.1109/TIP.2003.819861 PMID: 15376593

32. Veraart J, Novikov DS, Christiaens D, Ades-Aron B, Sijbers J, Fieremans E. Denoising of diffusion MRI using random matrix theory. NeuroImage. 2016; 142:394–406. https://doi.org/10.1016/j.neuroimage.2016.08.016 PMID: 27523449

33. Foi A, Boracchi G. Foveated self-similarity in nonlocal image filtering. In: Human Vision and Electronic Imaging XVII. vol. 8291. International Society for Optics and Photonics; 2012. p. 829110.

34. Baselice F. Ultrasound image despeckling based on statistical similarity. Ultrasound in Medicine and Biology. 2017; 43(9):2065–2078. https://doi.org/10.1016/j.ultrasmedbio.2017.05.006 PMID: 28651920

35. Chen G, Zhang P, Wu Y, Shen D, Yap PT. Denoising magnetic resonance images using collaborative non-local means. Neurocomputing. 2016; 177:215–227. https://doi.org/10.1016/j.neucom.2015.11.031 PMID: 26949289

36. Chen G, Wu Y, Shen D, Yap PT. Noise Reduction in Diffusion MRI Using Non-Local Self-Similar Information in Joint x-q Space. Medical Image Analysis. 2019;In Press. https://doi.org/10.1016/j.media.2019.01.006

37. Chen G, Dong B, Zhang Y, Shen D, Yap PT. Neighborhood matching for curved domains with application to denoising in diffusion MRI. In: Medical Image Computing and Computer-Assisted Intervention (MICCAI). Springer; 2017. p. 629–637.

38. Yang Z, Chen G, Shen D, Yap PT. Robust Fusion of Diffusion MRI Data for Template Construction. Scientific Reports. 2017; 7(1):12950. https://doi.org/10.1038/s41598-017-13247-w PMID: 29021588

39. Chen G, Dong B, Zhang Y, Lin W, Shen D, Yap PT. Angular Upsampling in Infant Diffusion MRI Using Neighborhood Matching in x-q Space. Frontiers in Neuroinformatics. 2018; 12:57. https://doi.org/10.3389/fninf.2018.00057 PMID: 30245622